Pre-Print Version

A Novel Framework for Predictive Modeling and Optimization of Powder Bed Fusion Process

Mallikharjun Marrey[1], Ehsan Malekipour[2†], Hazim El-Mounayri[3], Eric J. Faierson[4], Mangilal Agarwal[5]
Purdue University, Indianapolis, IN 46202, USA [1, 2, 3, 5]
Collaborative Additive Manufacturing Research Initiative (CAMRI) [1, 2, 3]
Quad City Manufacturing Laboratory-Western Illinois University, Rock Island, IL 61201, USA[4]

Abstract
Powder bed fusion (PBF) process is a metal additive manufacturing process which can build parts with any complexity from a wide range of metallic materials. PBF process research has predominantly focused on the impact of only a few parameters on product properties due to the lack of a systematic approach for optimizing a large set of process parameters simultaneously. The pivotal challenges regarding this process require a quantitative approach for mapping the material properties and process parameters onto the ultimate quality; this will then enable the optimization of those parameters. In this study, we propose a two-phase framework for optimizing the process parameters and developing a predictive model for 316L stainless steel material. We also discuss the correlation between process parameters -- i.e., laser specifications -- and mechanical properties and how to achieve parts with high density (> 98%) as well as better ultimate mechanical properties. In this paper, we introduce and test an innovative approach for developing AM predictive models, with a relatively low error percentage of 10.236% that are used to optimize process parameters in accordance with user or manufacturer requirements. These models use support vector regression, random forest regression, and neural network techniques. It is shown that the intelligent selection of process parameters using these models can achieve an optimized density of up to 99.31% with uniform microstructure, which improves hardness, impact strength, and other mechanical properties.

Keywords: Additive manufacturing, powder bed fusion, optimization framework, predictive models, neural network, intelligent parameters selection, energy density optimization, mechanical properties optimization.

1. Introduction

With Industry 4.0, the application of advanced manufacturing technologies integrated with information management technologies has flourished rapidly. This integration has created smart manufacturing processes which plays an important role in topology optimization, increasing cost efficiency, decreasing manufacturing lead time, and producing a superior buy-to-fly ratio in the rising economic competitiveness [1, 2]. Smart factories combine the physical world with the cyber world to fulfill such objectives (see Figure 1 for a schematic of smart factories).

With the increasing demand for mass customization in different industries, developing a precise predictive model is an essential prerequisite for controlling process parameters in complex advanced manufacturing techniques such as additive manufacturing (AM). This will help in the manufacturing of customized, topologically optimized parts with lower weight and better mechanical properties. In the fabrication of metal components, the powder-bed fusion (PBF) process has been proven to manufacture complex free-form parts with better mechanical properties than traditional manufacturing [3, 4].

The increasing demand and interest in the application of AM in such industries as aerospace, defense, and biomedical have led to significant research aimed at standardizing the AM process. However, multiple challenges exist, in particular, understanding the influence of the large number of process parameters involved in AM. There are more than 100 process parameters that influence the ultimate part quality [5-7]. Among all of those, there are only a few controllable parameters that significantly affect the part quality [3, 8] and lead to the formation of in-process defects such as microstructural -- porosity, balling, keyhole formation, cracks, etc. --, geometric and dimensional, and surface finishing defects [3]. These anomalies substantially weaken the ultimate mechanical properties of manufactured parts [4].

The full potential of AM cannot be achieved without controlling these parameters. Scholars can leverage the understanding and recognition of the influence of process parameters on the process defects and the mechanical properties in order to control of the process efficiently. This objective can be achieved by studying the process parameters, material properties, defects formation, and mechanical properties, and then mapping them together. Developing such a benchmark can provide a complete understanding of the defect formation and lead to the development of a precise predictive model for adjusting process parameters and obtaining the desired properties of manufactured part and, consequently, standardizing the process.

To date, no work has reported the ability to model and predict the influence of *multiple process parameters* on microstructure, densification, surface roughness, fabrication time, and mechanical properties *simultaneously*. On the other hand, scholars have not agreed about what constitute the most influential or significant parameters to optimize a given objective function. For instance, scholars reported 104 J/mm3, 70-120 J/mm3, 70- 95 J/mm3 as the optimum values of volumetric energy density (VED) for SS316L material [9-11]. Similarly, some literature introduced hatch space as the most influential parameter on the formation of porosity and tensile strength while few scholars proposed that hatch space does not affect the defect generation and mechanical properties [12-14]. Similarly, the knowledge of the influence of beam diameter is limited when it varies along with other controllable parameters. We address these challenges by proposing and demonstrating a systematic approach for modeling and optimizing the process to achieve build consistency with controlled mechanical and microstructural properties.

Although PBF technology has significantly developed and is employed in different industries, many challenges have remained. These challenges hinder process repeatability,

†Corresponding author (emalekip@purdue.edu)

Preprints (www.preprints.org) | NOT PEER-REVIEWED | Posted: 13 October 2021 doi:10.20944/preprints202110.0192.v1

consistency, and stability. Numerous research studies regarding the influence of process parameters on the ultimate quality of fabricated parts for different materials and machines have been conducted. These have revealed that it is very difficult to control all aspects of the process or even to evaluate the collective influence of all parameters on the properties of fabricated parts. Scholars focused on identifying the influence of only a few process parameters -- predominantly laser specifications -- on the surface quality, process signatures, or particular mechanical properties of printed components [15, 16]; the ultimate quality was predominantly correlated with a single parameter only. A systematic approach for optimizing all controllable parameters while mapping the process parameters and material properties onto the ultimate properties of the fabricated parts is critical to achieve a near-flawless fabrication process.

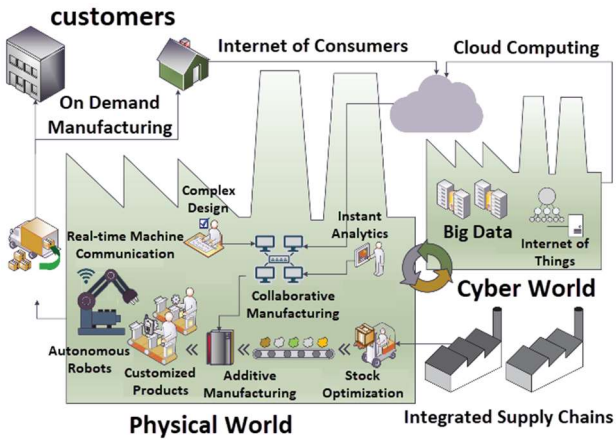

Figure 1: Schematic of general properties required in industry 4.0 [1].

Providing a predictive model is a significant notion for achieving smart manufacturing, which is the key for a transformative development in product fabrication. For instance, in orthodontic treatment altering the material properties in a designed mouthpiece results in different force magnitude, location, and distribution applied on mandibular central incisor and mandibular canine [17]. To develop a predictive model for a process, a comprehensive interpretation of the relationship between the process parameters, defects, and ultimate quality of the manufactured part is vital. PBF lacks such an efficient approach that can facilitate the avoidance or significant minimization of defect generation and mechanical property anomalies by governing the process parameters. This research proposes a framework for studying the influence of process parameters on multiple properties of the manufactured part, optimizing the parameters for improving the ultimate quality of the part and developing a predictive model of the process by training a machine learning (ML) algorithm – support vector regression, random forest regression – and an artificial neural network (ANN) with back-propagating algorithm.

This research addresses the above-mentioned challenges by achieving five objectives:

a. Proposing a framework for optimizing the PBF process parameters.

b. Understanding the influence of laser power and scan speed on the porosity and density of fabricated samples and optimizing the VED for achieving maximum density (Phase I of the proposed framework).

c. Studying and optimization of the combined influence of laser power, scan speed, hatch space, and beam diameter on microstructural properties, mechanical properties (hardness, impact strength, and tensile strength) and surface roughness. (Phase II of proposed framework). This is achieved using DOE (Design of Experiments).

d. Mapping the material properties and process parameters onto the ultimate properties of the manufactured samples by using ML.

e. Developing a predictive model for intelligent selection of process parameters and achievement of the desired quality properties by using different ML techniques, namely, SVR, Random Forest Regression, and FFBP Neural Network, with limited quantitative data.

2. Methodology: Developing a Two-phase Framework and Predictive Models

In-process defects -- such as porosity, crack formation, etc. -- are amongst the most prevalent defects encountered by manufacturers. Uncertainty in selection of laser power, scan speed, hatch spacing, and VED for printing parts with different materials are the main contributing parameters for formation defects during the manufacturing process. The formation of defects decreases the density through irregular porosity distribution which, in turn, affects the mechanical properties and quality characteristics of the manufactured part.

In this work, we implemented a two-phase framework for optimizing the process parameters. In phase I, we conducted the first set of experiments to achieve more insight into densification and porosity formation as well as to attain maximum density by minimizing porosity. These experiments provided the optimized range for VED to be used in the next phase.

In phase II, we studied the effects of a set of process parameters on the mechanical properties and quality characteristics by running the second set of experiments within the optimized VED range obtained from phase I. The objective of this phase was to understand the correlation between process parameters, material properties, and ultimate quality characteristics of printed parts. By employing the results from phase II, a predictive model was developed for intelligent selection of process parameters according to the desired quality properties.

2.1. Proposed Framework

To address the challenges and gaps mentioned above, we are introducing a two-phase framework for establishing the correlation between process parameters and the ultimate properties of manufactured parts. Figure 2 shows the proposed framework to standardize the process of studying and optimizing the process parameters, reducing inconsistency in results for a given material, and developing an innovative predictive model for intelligent selection of process parameters, with emphasis on the different ML techniques, error rate, uncertainty of the data, and predictions algorithm.

2.2. Phase I

Preprints (www.preprints.org) | NOT PEER-REVIEWED | Posted: 13 October 2021 doi:10.20944/preprints202110.0192.v1

Achieving maximum density is the first prerequisite for manufacturing flawless parts by metal AM. Hence, the main objective of phase I was to achieve maximum density. In this phase, we considered altering only laser power and scan speed and studied the resulting microstructure in the first set of printed samples in order to obtain the optimum range for VED. This optimized range of VED was later employed in phase II for studying the effects of other process parameters on the mechanical and quality characteristics of the second set of samples printed within their maximum densification range.

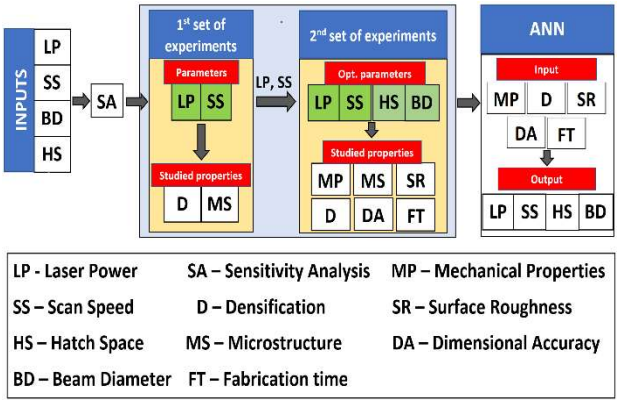

Figure 2: The proposed framework and corresponding workflow for developing the ANN model.

2.2.1. Material and Equipment

316L stainless steel (SS) was used in this research. 316L SS has widespread application in additive manufacturing given its high tensile strength at high temperatures, high hardness, toughness, and corrosion resistance properties [4]. In this work, samples were manufactured with a constant layer thickness of 20 µm using an EOS M270 3D printer.

2.2.2. Mathematical Modeling

For any AM process, the first step is to determine the accurate process parameters for successful completion of the manufacturing process. In thermal AM processes such as PBF, process parameters are predominantly adjusted by evaluating the VED (i.e., the amount of heat flux given per unit volume) which is required for the sintering/melting of the powder feedstock. Substantial research has been conducted by scholars to identify the best range of VED values for SS 316L. Scholars obtained a diversified range of values for the same material processed using PBF (see Figure 3).

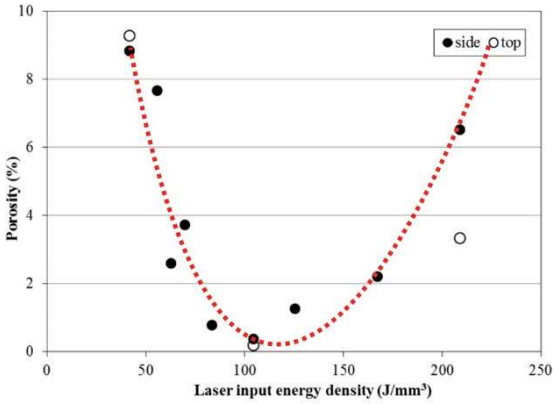

Figure 3: VED benchmark provided in [18].

We first estimated the range of VED values for SS 316L in PBF then conducted experiments to obtain the optimized range to achieve maximum density. A rough VED required for successful melting and consequent solidification can be estimated based on the heat per unit volume -- q (J/mm3) -- in Eq. 1.a [19]

$$\boldsymbol{q = [c.\Delta T + l_f]\rho} \qquad \text{Eq. 1.a}$$

$$\boldsymbol{\Delta T = T_m - T_0} \qquad \text{Eq. 1.b}$$

where c (J/Kg.K) is the specific heat capacity, l_f (J/Kg) is the latent heat of fusion, ρ (Kg/mm3) is the density of the powder material in Eq. 1.a and T_m (K) and T_0 (K) are the melting temperature of the material and room temperature, respectively, in Eq. 1.b.

To consider various thermal phenomena [20] associated with PBF process, an efficiency coefficient η is incorporated, which accounts for heat losses due to the reflectivity of the powder, heat conduction, and additional losses. Eq. 2 shows the VED equation considering the efficiency coefficient

$$\boldsymbol{VED = \frac{q}{\eta} = \frac{q}{(1-R_P)(1-k_{rel})\eta^*}} \qquad \text{Eq. 2}$$

where R_P and k_{rel} are the reflectivity of the powder feedstock material and relative thermal conductivity of the feedstock material respectively. η^* is an additional efficiency factor assumed to be 0.20 [19].

Table 1: Property values for SS316L.

Property	Value
Specific heat capacity, c (J/Kg.K)	500
Melting temperature, T_m (K)	1673
Latent heat of fusion, l_f (J/kg)	0.25
Density, ρ (Kg/mm3)	7.99 x 10^{-6}

By substituting the SS316L properties values (see Table 1) in Eq. 1a, the heat flux was obtained as

$$\boldsymbol{q = 5.50\ \frac{J}{mm^3}} \qquad \text{Eq. 3.a}$$

Substitution of the obtained heat flux from Eq. 3.a in Eq. 2 produces VED:

Preprints (www.preprints.org) | NOT PEER-REVIEWED | Posted: 13 October 2021 doi:10.20944/preprints202110.0192.v1

$$VED_{R_P=0.05} = 57.89\ \frac{J}{mm^3} \quad \text{Eq. 3.b}$$

$$VED_{R_P=0.6} = 137.5\ \frac{J}{mm^3} \quad \text{Eq. 3.c}$$

The obtained VED values using Eq. 3.b and Eq. 3.c were considered as the lowest and highest limits for the design of experiments (DOE) in which the VED varied ±10%.

2.2.3. Sensitivity Analysis

Sensitivity analysis (SA) quantifies the correlation between a given model and its input parameters [21]. The main objective of conducting SA is to understand which inputs contribute most to output variability [21]. Another function to model VED (Eq. 4) is based on the commonly cited controllable parameters in PBF, namely, laser power (LP), scan speed (SS), layer thickness (LT), and hatch space (HS). In fact, these parameters have a significant influence on the ultimate quality of manufactured parts [3, 8, 22, 23]. We employed SA to evaluate the correlation of the laser specifications (i.e., LP, SS, and HS) with VED from Eq. 4 while kept the layer thickness constant.

$$VED = \frac{LP}{HS \times SS \times LT} \quad \text{Eq. 4}$$

We used Fourier Amplitude Sensitivity Testing (FAST) -- a variance-based global sensitivity analysis method, which is based on conditional variance to determine the sensitivity within the range of 0 to 1. The SA results showed that scan speed drastically changes the energy density, hence, it might predominantly influence the ultimate properties of the fabricated part. Similarly, laser power and hatch spacing had considerable effects while the effect of layer thickness was zero since it was set to a constant value. We assigned the number of levels -- number of values assigned in the parameters' range -- according to the parameters' sensitivity. Figure 4 shows the values of the ultimate global sensitivity coefficients obtained by SA. Previous literature also confirmed the significant influence of laser power and scan speed as the two main parameters on the ultimate quality of the printed part [24].

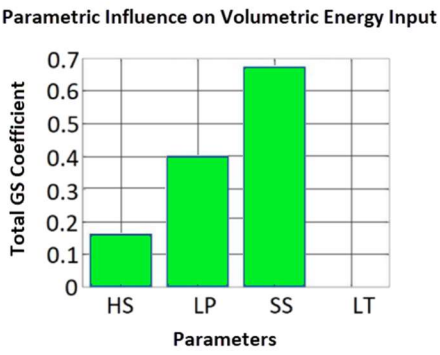

Figure 4: Total Global Sensitivity (GS) Coefficient.

2.2.4. Design of Experiments for Phase I

In this phase, we employed full factorial analysis for designing the experiments. Table 2 shows the parameters -- laser power and scan speed -- whose values were assigned based on the estimated VED in section 2.2.2 and the benchmarks provided in literature [25-28]. For the first set of experiments, we printed 10×10×5 mm^3 samples considering only laser power and scan speed while hatch space (HS) and beam diameter were kept constant at their machine default values (HS = 0.09 mm and BD = 0.2mm).

In this phase, we studied the microstructure, porosity, and densification of the printed samples to map them onto the VED values. Previous literature demonstrated that the porosity generated during the process significantly affects the mechanical properties of manufactured parts. The literature shows that low porosity formation in near fully dense parts substantially enhanced mechanical properties and build consistency [29, 30]. Therefore, we sought the optimal range of energy density for maximum densification in this phase. It should be noticed that we studied only 13 of 16 total samples due to similar energy density of sample 2 to 8, sample 6 to 12, and sample 9 to 14.

Table 2: Full factorial DOE.

No	LP, W	SS, m/s	VED, J/mm3	No	LP, W	SS, mm/s	VED, J/mm3
1	100	700	79.36	9	150	700	119.05
2	100	800	69.44	10	150	800	104.17
3	100	900	61.73	11	150	900	92.59
4	100	1000	55.56	12	150	1000	83.33
5	125	700	99.21	13	175	700	138.89
6	125	800	86.81	14	175	800	121.53
7	125	900	77.16	15	175	900	108.02
8	125	1000	69.44	16	175	1000	97.22

2.3. Phase II

From phase I, the optimized range of VED values was obtained for achieving maximum densification. In the second phase, laser power, scan speed, hatch space, and beam diameter were studied to unveil the correlation of the process parameters with ultimate mechanical and quality properties of the manufactured part. We discuss details about the parameter selection, DOE, mechanical testing along with the data analysis in the Results and Discussion section.

2.3.1. Design of Experiments for Phase II

In this phase, we considered four process parameters -- laser power, scan speed, hatch space, and beam diameter -- with different levels. We employed the Taguchi method to optimize the DOE instead of conducting a more expensive full-factorial analysis. Table 3 shows the levels and level values assigned to each parameter based on the results obtained from phase I. Table 4 shows the resulting Taguchi DOE. For each set of parameters, a sample was printed and different mechanical tests -- namely tensile, impact, and hardness -- were performed. For tensile and impact tests, the samples were designed according to ASTM E8 and ASTM E23 standards [31].

Table 3: Control factors and levels for Taguchi DOE.

Factor	Level values	Levels
LP (W)	125, 150, 175, 195	4
SS (mm/s)	700, 800, 900, 1000, 1100, 1200	6
HS (mm)	0.09, 0.12, 0.15	3
BD (mm)	0.1, 0.15, 0.2	3

Table 4: Taguchi DOE.

No	LP (W)	SS (mm/s)	HS (mm)	BD (mm)
1	125	700	0.09	0.1

Preprints (www.preprints.org) | NOT PEER-REVIEWED | Posted: 13 October 2021 doi:10.20944/preprints202110.0192.v1

2	125	800	0.09	0.2
3	150	700	0.12	0.15
4	150	800	0.09	0.2
5	150	900	0.09	0.1
6	175	700	0.12	0.2
7	175	800	0.12	0.1
8	175	900	0.09	0.15
9	175	1000	0.09	0.2
10	175	1100	0.09	0.1
11	195	700	0.15	0.15
12	195	800	0.12	0.15
13	195	900	0.12	0.2
14	195	1000	0.09	0.1
15	195	1100	0.09	0.2
16	195	1200	0.09	0.15

2.3.2. Signal-to-noise Ratio and Analysis of Variance

Signal-to-noise (S/N) ratio is used as a quality indicator that evaluates the influence of the process parameters on the ultimate properties. The S/N ratio is calculated at three levels: lower-the better, nominal-the-better, and higher-the-better. S/N value was calculated in phase II for all 16 experiments and the effects plot for S/N ratios and means of optimized parameters was represented for each parameter at their assigned levels using Taguchi method, generated by Minitab® (See sub-section 3.2.1 for S/N results of surface roughness). Finally, the variance was calculated based on the resulting S/N values by applying Analysis of Variance (ANOVA).

ANOVA is a statistical method evaluating the variance of properties within the tested range of levels for each process parameter in comparison with the total variance of all parameters to express the percentage contribution (Cntb%) of each process parameter. The relative percentage contribution among the process parameters is determined by comparing the relative variance using adjusted sum of square (A.SSq), adjusted mean square (A.MS), P-values (P-val.), and F-values (F-val.) [32].

The combination of S/N and ANOVA helped obtain the optimal range of process parameters and also revealed the correlation between the material properties, process parameters, and ultimate properties of SS 316L parts printed by PBF. In addition, this combination makes it possible to understand the significance of each parameter within the employed range.

2.3.3. Mechanical Testing

To understand the correlation between process parameters and quality properties of the printed samples, a series of mechanical tests –surface roughness, hardness, Charpy impact, and tensile tests -- was conducted.

The surface roughness (R_a) measurement was carried out on Bruker DektakXT. A stylus of 2µm-radius was used with the profile set to hills and valleys and with a range of 6.5 µm, force of 5 mg, speed of 600 µm/s, and time duration of 25 seconds. Three surface profiles with the scan length of 10 mm were measured for each sample on two sides and the center of samples R_a value was calculated from the profile by using equation 5

$$\boldsymbol{R_a} = \frac{\mathbf{1}}{\boldsymbol{L}} \int_0^{\boldsymbol{L}} |\boldsymbol{Y(x)}| \boldsymbol{dx} \qquad \text{Eq. 5}$$

where R_a is defined as the arithmetic average deviation of hills and valleys from the mean line, L is the scan length, and Y(x) is the curvature profile.

The hardness test was conducted on a Rockwell hardness testing machine B scale equipped with a 1/16-inch steel ball; a 100-Kgf force was applied. We conducted the hardness test to achieve more insight into the resistance of material for plastic (or permanent) deformation for different sets of parameters.

For the **Charpy impact test,** the specimen was loaded, and the position of the specimen was adjusted such that the notch was parallel and centered to the pendulum. The pendulum was dropped electronically to avoid any losses due to vibrations. The equipment was not bolted to the ground, which might affect the results with variances of ± 5 J. The objective of conducting the impact test was to study the amount of absorbed energy and the effect of process parameters on the strength of the printed samples.

The Tensile test was conducted on a Jinan Dual column Universal testing Machine, with a pancake type load cell of 20KN, at the room temperature. The yield strength (YS), elongation, and ultimate tensile strength (UTS) were obtained for each experiment. The objective of conducting the tensile test was to study the mechanical behavior (strength, ductility etc.) of the part under uniaxial load conditions. This will help in quality control of the material for specific applications.

2.4. Predictive Modeling

PBF process is inherently a complex process with more than 100 different process parameters involved [5-7]. Previous literature studied the impact of each parameter on the quality properties and developed a one-to-one correlation between the selected parameter and property of interest; however, those estimations could not provide a comprehensive relationship between a process parameter and multiple part quality properties. For instance, increasing scan speed reduces the average surface roughness (for speed lower than 15 mm/s) and thermal shrinkage which are positive effects while increases in melt pool instability causes deeper longitudinal cracks on scanning tracks –which is a negative effect [33, 34] .

To obtain an optimum quality printed part, the correlation between "a set" of process parameters and the resulting properties is required. To fulfill such an objective, one scenario is to develop a physics-based model to predict the quality properties according to the parameters. The scholars' previous attempts have been unsuccessful for developing a comprehensive analytical model due to the complex non-linear nature of the process. Alternatively, a data-driven modeling based on empirical benchmarks and statistical theories was developed [32].

In this work, we employed three different methods -- support vector regression (SVR), random forest methods in machine learning (ML), and ANN -- to develop practical predictive models and correlate different process parameters to different ultimate quality properties. We will discuss these techniques, and identify the best one based on multiple criteria, including error rate, loss function, uncertainty, and stability.

2.4.1. Support Vector Regression

SVR is a type of ML that can be used for regression problems. Using SVR, a hyperplane was identified so that the maximum number of data points fell within that boundary (maximal margin). Instead of eliminating/reducing the error rate -- as carried out in simple linear regression -- SVR adjusts the error within a certain threshold. Our objective in SVR was to keep the maximum points within this margin. The best fit line was the hyperplane with the highest number of points within the boundaries.

Preprints (www.preprints.org) | NOT PEER-REVIEWED | Posted: 13 October 2021 doi:10.20944/preprints202110.0192.v1

2.4.2. Random Forest Regression

Random forest regression (RFR) is one of the supervised learning techniques used for both classification and regression model training. In this technique, the training data is divided into several groups -- called trees or bagging -- and the model runs in each tree. The final prediction is the average of the values generated by each tree. Using the average reduces the uncertainty of the model. As a result, variation in error rate is greatly reduced because error in one data set will not significantly affect the final predicted output. The only possibility for a wrong prediction is if more than half of the data is deceptive. This lower uncertainty is the major advantage of models developed by RFR compared with other techniques such as SVR and NN.

2.4.3. Neural Network

ANN is a supervised ML technique that can be employed for regression problem effectively. This technique is suitable for PBF process due to non-linear complex correlation between the input and output data (i.e., process parameters and quality characteristics). In this work, a multi-layer feed-forward back-propagating (FFBP) neural network (NN) was developed with laser power, scan speed, hatch space, and beam diameter as features/inputs and ultimate tensile strength (UTS) and surface roughness as labels/outputs (Figure 5). To train the model, we employed one hidden layer with three nodes and used the experimental results acquired from the framework as the training data. The weights were calculated and adjusted by backpropagation (BP) method, which gradually reduces the gap between the generated and expected output (actual experimental output).

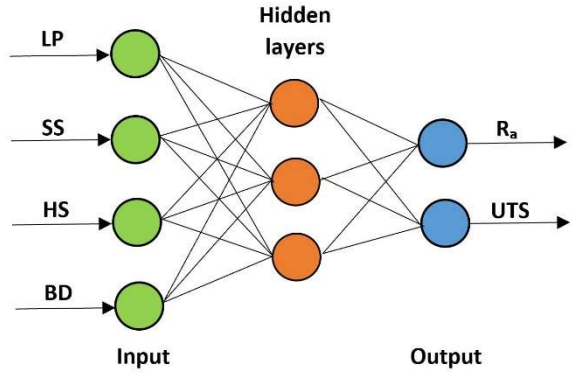

Figure 5: The schematic for ANN architecture of this research.

We employed sigmoid function in python for developing our ANN model. Since this function varies between 0 to 1, the input and output were normalized between 0 and 1 (see table 15-18). The activation function makes the training of weights easier for sigmoid function. The network is forwarded from input to output by assigning some random values and then BP uses a loss function for calculating the error between the computed value and the target value. The loss function is calculated by the mean sum squared loss function shown in Eq. 6 [35]

$$\boldsymbol{Loss} = \sum(\mathbf{0.5})(\boldsymbol{o}-\boldsymbol{y})^{\mathbf{2}} \quad \text{Eq. 6}$$

where o is the predicted output and y is the actual output. The function was trained individually for each output (quality characteristics). In the last step, a multi-input multi-output NN was trained to provide a model correlating all inputs to all outputs.

3. Results and Discussion

In section 2, we explained the methodology of implementing a two-phase framework for developing a predictive model in PBF process. In this section, we discuss the results obtained from each phase and try to establish a correlation between process parameters and the ultimate quality properties of the printed samples. In addition, we assess the different predictive models, including their efficiency based on the minimum error rate.

3.1. Phase I: Results and Discussion

The VED minimum and maximum values were obtained as 57.89 and 137.5 J/mm^3, respectively, using the mathematical model described in subsection 2.2.2. In subsection 2.2.3, SA was conducted to study the influence of laser power, scan speed, and hatch space on VED. The results showed that scan speed had the highest impact on VED, followed by laser power and hatch space respectively. After SA, samples were printed according to the DOE for phase I, introduced in subsection 2.2.4. We cut each sample in the middle -- both perpendicular and parallel to the build direction (Figure 6) -- by using wire electric discharge machining (WEDM) process. WEDM process was chosen because of its capability of machining electrically conductive hard materials without inducing any stresses or impact.

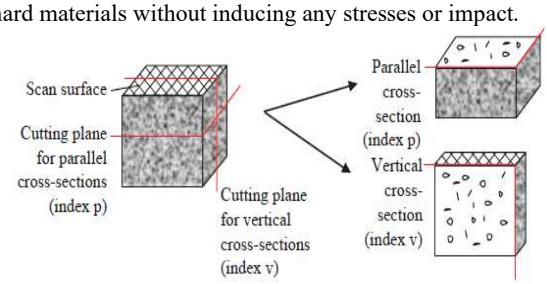

Figure 6: WEDM cutting planes through specimens from phase I.

Then, we took sixteen micrographs in total from each sample by using a scanning electron microscope (SEM), six micrographs from the horizontal cross-section -- each corner plus two from the center -- and two from the vertical cross-section. We used two different magnifications -- 60X and 300X (100µm and 10µm scale, respectively) – for each micrograph and then employed MATLAB image processing to measure the porosity of each sample in three steps (Figure 7). First, we generated bi-color black and white images from each micrograph; second, the threshold level was adjusted by comparing the pore size between the SEM image and the MATLAB-generated image to increase the method accuracy [36]; finally, we obtained the porosity percentage by calculating and averaging the ratio of black parts (pores) to the white parts in the micrographs related to each cross-section [37].

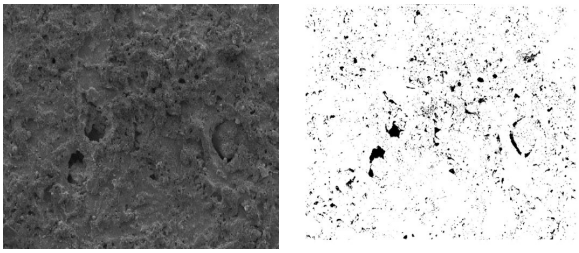

Preprints (www.preprints.org) | NOT PEER-REVIEWED | Posted: 13 October 2021 doi:10.20944/preprints202110.0192.v1

Figure 7: a. Micrograph; b. Bi-color micrograph with adjusted threshold level.

By analyzing the horizontal cross-section, we revealed three different types of porosity – low, medium, high -- according to the level of VED. In the first type, low VED led to incomplete melting of the powder particles and formation of irregular pores due to lack of fusion (LOF) (Figure 7.a). In the second type, exposure of the samples to high VED vaporized the material and formed circular gas pores (Figure 7.b). These pores could be either the cross-section of a keyhole or a simple circular pore. The type of pores could be detected by analyzing the vertical micrographs. In the third type, the samples gained from exposure by medium VED possessed microscale holes with a nearly uniform distribution throughout the cross-section. These samples depicted better mechanical properties compared to other types [38]. Vertical cross-sections, on the other hand, illustrated less frequent but bigger size porosity, which usually were propagated through layers underneath. Table 5 illustrates the porosity percentage of the samples shown in Figure 8. The results were in close agreement with the results from previous literature [18].

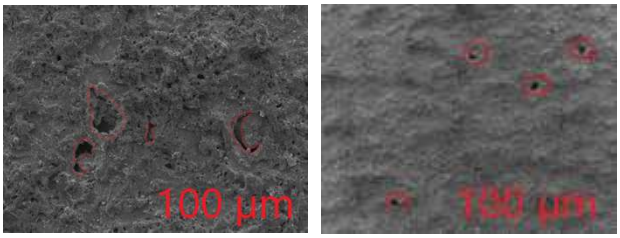

Figure 8: a. LOF pores (the low VED with LP 100 W and SS 900 mm/s); b. gas pores (the highest VED with LP 175 W and SS 700 mm/s).

As Figure 9 depicts, we printed the samples with the range of VED altered between 55 and 138 J/mm^3. This VED range created parts with a density between 95.52% and 99.31% and a maximum of 99.31% by VED of 99.2 J/mm^3. Considering the density percentage, we could narrow the range of optimum VED -- the green band in Figure 9 -- to 90 and 105 J/mm^3. This suggested that the optimized range of laser power is 150 to 200 W while the optimized range of scan speed is 800 to 1000 mm/s. These ranges were employed as the inputs for phase II in our next step.

Table 5: The porosity percentage of the samples.

VED (J/mm^3)	Horizontal	Vertical	Average
61.7	5.453%	3.5%	4.48%
97.2	0.879%	0.5%	0.69%
138	1.875%	1.31%	1.59%

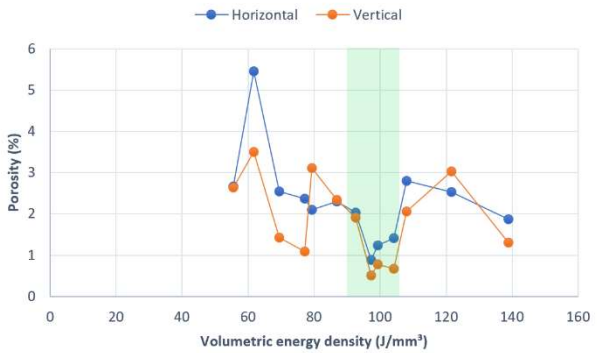

Figure 9: Porosity vs VED.

3.2. Phase II: Results and Discussion

In phase II, we studied the correlation between material properties, process parameters -- laser power, scan speed, hatch space, and beam diameter -- and ultimate quality characteristics of manufactured parts within the maximum range of densification.

3.2.1. Surface Roughness

Surface roughness measurement was conducted on the Bruker DektakXT system. Three profiles with 10mm-scan length were read and the average roughness (R_a) was calculated for each sample. We obtained Y(x) from each profile (see Figure 10) and R_a was calculated using Eq. 5.

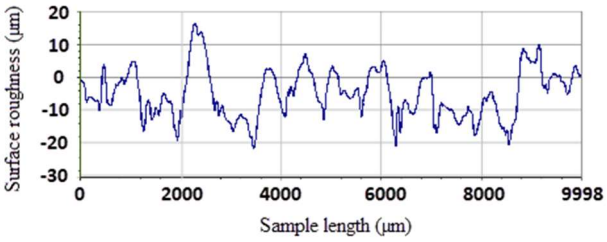

Figure 10: Profile of 10mm scan.

Table 6: Obtained surface roughness for DOE in phase II.

No.	Left (um)	Center (um)	Right (um)	Average
1	20.31	18.94	27.22	22.16
2	17.39	23.2	14.13	18.24
3	22.34	17.39	11.56	17.1
4	17.61	13.07	16	15.56
5	14.12	15.84	11.68	13.88
6	14.44	18.25	17.98	16.89
7	13.3	16.29	16.26	15.28
8	13.52	24.39	14.75	17.55
9	15.85	16.11	14.44	15.47
10	14.28	18.89	15.88	16.35
11	10.79	15.78	14.99	13.85
12	20.98	19.71	18.36	19.68
13	10.6	21.04	9.83	13.82
14	11.26	14.82	11.68	12.59
15	16.05	12.87	14.5	14.47
16	11.18	13.2	9.49	11.29

Preprints (www.preprints.org) | NOT PEER-REVIEWED | Posted: 13 October 2021 doi:10.20944/preprints202110.0192.v1

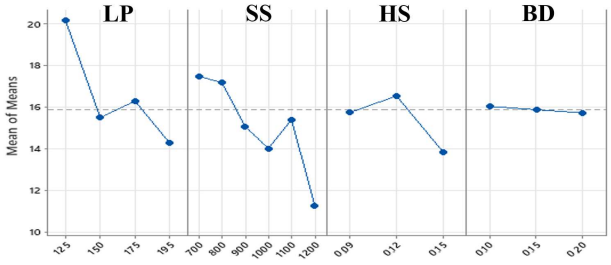

Figure 11: Trend of process parameters influence on R_a represented by main effects plot of means.

Table 6 presents the average roughness values for the set of all DOE. The main effect plot of means – based on S/N ratio (the lower-the-better) analysis -- was represented in Figure 11. The analysis of the average surface roughness in this figure reveals that R_a decreased with the increase in scan speed or laser power. ANOVA evidenced that in a process with multiple varying parameters, scan speed and laser power followed by hatch space and beam diameter have the highest impact on the roughness within the optimum VED range respectively (Table 7), which corroborates the results of the S/N analysis.

Table 7: ANOVA for surface roughness vs LP, SS, HS & BD.

Source	DF	A.SSq	A.MS	F-val.	P-val.	Cntb %
LP	3	18.65	6.215	1.65	0.346	21.37
SS	5	28.31	5.663	1.50	0.392	32.45
HS	2	15.60	7.802	2.07	0.310	17.88
BD	2	13.38	6.690	1.77	0.272	15.33
Error	3	11.31	3.770			
Total	15	87.25				

3.2.2. Hardness

We calculated HRB (Rockwell Hardness B Scale) by taking the average of three readings, one from each side and one from the center of each sample. Table 8 shows the calculated HRB and S/N ratio (the higher-the-better) for all samples. The results show that the hardness value was almost constant (with ±5 variance), irrespective of the set selection of individual parameters as long as VED fell within the optimized range and was corroborated by the nearly constant S/N value. Thus, we needed neither calculate ANOVA nor to train a predictive model for hardness test.

Table 8: S/N ratios for samples with different hardness values.

Sample	HRB	S/N ratio	Sample	HRB	S/N ratio
1	86.6	38.75	9	91	39.18
2	94.8	39.54	10	91.5	39.23
3	93.23	39.39	11	88.57	38.95
4	93.67	39.43	12	92.23	39.3
5	89.13	39.00	13	89.47	39.03
6	89.9	39.07	14	89.5	39.04
7	89.6	39.05	15	92.87	39.36
8	93.03	39.37	16	93.6	39.42

3.2.3. Charpy Impact Test

The impact test was conducted on all 16 samples in phase II and the results were presented in Table 9. S/N ratio (the higher-the-better) was calculated, and the main effect plot of means is represented in Figure 12. In general, the result demonstrated that within the study range of parameters, increasing scan speed elevated the impact strength, whereas, increasing laser power and hatch space decreased the impact strength of the samples. The best Charpy impact was obtained for the sample with the lowest beam diameter. ANOVA was also conducted to calculate the P-value, which illustrates the effect of each process parameter on the impact strength presented in Table 10. The results demonstrate that the influence of a parameter on the strength of the printed samples is in the following order: hatch space, laser power, scan speed, and then beam diameter.

Table 9: Impact test results for all 16 samples in phase II.

Sample	Impact strength (J)	Sample	Impact strength (J)
1	148	9	137.2
2	144	10	143.8
3	127.5	11	109.5
4	136.5	12	120.5
5	150.2	13	126.2
6	124	14	140
7	129.6	15	134.2
8	134.5	16	132.2

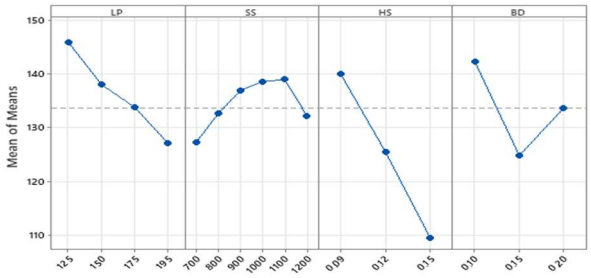

Figure 12: Trend of process parameters influence on impact strength represented by main effect plot of means.

Table 10: ANOVA for impact strength vs LP, SS, HS & BD.

Source	DF	A. SSq	A.MS	F-val.	P-val.	Cntb. %
LP	3	50.12	25.06	13.72	0.028	27.06
SS	5	30.40	11.20	7.50	0.012	16.46
HS	2	78.49	26.16	14.32	0.031	42.38
BD	2	20.70	8.140	4.46	0.009	11.18
Error	3	5.48	1.827			
Total	15	185.2				

3.2.4. Tensile Test

The tensile test was conducted to study the influence of process parameters within the optimized range on the mechanical behavior of the printed samples. Figure 13 shows the main effect plot of means plotted to each process parameter with individual levels while Table 11 shows the UTS values and their respective S/N ratio. The maximum UTS of 808.52 MPa was achieved at the VED of 98.48 J/mm³ which is higher than the UTS achieved by conventional manufacturing [39].

Table 11: Obtained UTS for DOE in phase II.

Sample	UTS	Sample	UTS
1	716.79	9	792.36
2	775.16	10	689.64
3	644.03	11	678.74
4	779.32	12	634.11
5	643.39	13	663.44
6	699.92	14	726.06
7	752.94	15	808.52

Preprints (www.preprints.org) | NOT PEER-REVIEWED | Posted: 13 October 2021 doi:10.20944/preprints202110.0192.v1

8	632.70	16	749.98

As shown in Figure 13, the results clearly demonstrate that LP, SS, HS, and BD have a significant effect on the UTS within the optimized range of VED. Following the S/N ratio, ANOVA was also conducted to calculate the P-value (Table 12). The results demonstrate that the influence of parameters within the tested range are in the following order: SS, BD, LP, and HS. No specific correlation was observed between these parameters and UTS; however, the results depict that the lower LP and HS generally resulted in higher UTS while it was higher SS and BD that resulted in higher UTS. More experiments need to be conducted to develop a complete correlation between the parameters and UTS.

Table12: ANOVA for UTS vs LP, SS, HS, & BD.

Source	DF	A. SSq	A. MS	F-val.	P-val.	Cntb. %
LP	3	73.47	17.2	0.32	0.400	22.34
SS	5	114.2	38.06	0.57	0.997	34.73
HS	2	36.58	5.26	0.13	0.186	11.12
BD	2	95.32	24.14	0.41	0.618	28.99
Error	3	9.24				
Total	15	328.8				

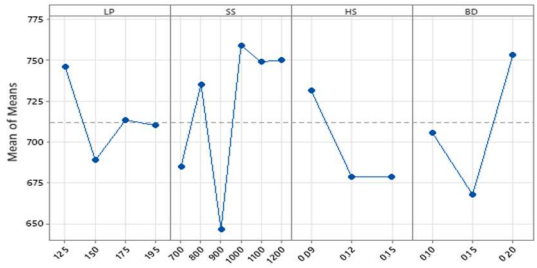

Figure 13: Trend of process parameters influence on UTS represented by main effect plot of means.

3.3. Predictive Modeling

3.3.1. Support Vector Regression

16 data sets were employed to develop an SVR predictive model - 13 sets for training and 3 sets for testing. To fulfill such an objective, we first conducted heatmap evaluation. Heatmap is an exhibition of correlation between inputs to detect dependencies. The heatmap is calculated using the coefficient of determination (R^2), which quantifies the proportion of variance in output properties in relation to the process parameters. Any correlation between 2 inputs with calculated value of R^2 above +0.5 or below – 0.5 demonstrates their dependency; thus, one of the inputs can be eliminated from the training set. Furthermore, the top half pair of inputs above the diagonal is neglected since it is a replica of the bottom half as well as the diagonal pairs since they represent the correlation between the same inputs. Such performance increases the efficiency of the predictions. We used a heatmap to investigate any possible correlation between the inputs in phase II before employing different techniques for developing predictive models. The results demonstrated no correlation between the inputs with obtained R^2 value of 0.4511. The second step was to develop the predictive model using SVR. After training the data, we conducted trial evaluation using the remaining 3 data sets to validate the model. Table 13 shows the predicted value and error percentage for surface roughness prediction for each set. The error percentage obtained varied between 12.92 and 34.47 with a mean error of 20.18%. We concluded this technique was not suitable for developing a predictive model for PBF process since it showed high error rate percentage and produced uncertain results.

Table 13: SVR method: actual vs predicted value for surface roughness.

Test data	Actual R_a	Predicted R_a	Error %
175,800,0.12,0.1	15.28	17.255	12.92
195,700,0.15,0.15	13.85	15.67	13.14
195,1000,0.09,0.1	12.59	16.93	34.47

3.3.2. Random Forest Regression

Out of the 16 data sets, 12 sets were assigned as training data and 4 sets as testing data. Training data was divided into three random groups called trees. The number of trees was selected by running the model with different numbers of trees -- 2 to 6 trees -- and among all the values, 3 trees generated a minimum error rate with better R^2. Table 14 shows the predicted vs. actual data. The results show that the error rate was between 23 to27% by considering only 12 sets of training data. More experimental data is needed to reduce this error rate.

Table 14: RFR method: actual vs. predicted value for surface roughness.

Test data	Actual R_a	Predicted R_a	Error %
175,800,0.12,0.1	15.28	19.35	26.64
195,700,0.15,0.15	13.85	17.122	23.624
195,1000,0.09,0.1	12.59	15.57	23.67

3.3.3. Neural Network

16 data sets were divided into 12 sets for training and 4 sets for testing. Test data is used to assess the trained network. The mean error rate is calculated by averaging the error rates from the test data. Two networks were developed to predict separately surface roughness and UTS. Table 15 and 16 show the error percentage of training data sets for surface roughness and UTS respectively. The results show the mean error rate of 10.236% with a loss rate of 0.0002946 for surface roughness network and the mean error rate of 7.53% with a loss rate of 0.000253 for The UTS network.

Table 15: Surface roughness: Actual vs predicted data with error percentage in multi-input single-output neural network.

Training data	Actual Ra/100	Predicted Ra/100	Error %
125,700,0.09,0.1	0.2216	0.21	5.2346
125 ,800 ,0.09 ,0.2	0.1824	0.169	7.3465
150 ,800 ,0.09 ,0.2	0.1556	0.168	7.9691
150 ,900, 0.09, 0.1	0.1388	0.1743	25.5764
175 ,700 ,0.12 ,0.2	0.1689	0.1819	7.6966
175,900,0.09,0.15	0.1755	0.1633	6.9515
175,1000,0.09,0.2	0.1547	0.1437	7.1105
175, 1100, 0.09, 0.1	0.1635	0.1482	9.3578
195 ,800 ,0.12 ,0.15	0.1968	0.1764	10.3658
195 ,900, 0.12, 0.2	0.1382	0.1539	11.3603
195, 1100,0.09,0.2	0.1447	0.134	7.3946
195,1200,0.09,0.15	0.1129	0.1315	16.4748

Table 16: UTS: Actual vs predicted data with error percentage in multi-input single-output neural network.

Training data	Actual UTS/1000	Predicted UTS/1000	Error %
125,700,0.09,0.1	0.7167864	0.693078	3.308
125 ,800 ,0.09 ,0.2	0.7751575	0.80191983	3.452

Preprints (www.preprints.org) | NOT PEER-REVIEWED | Posted: 13 October 2021 doi:10.20944/preprints202110.0192.v1

150 ,800 ,0.09 ,0.2	0.7793171	0.75758627	2.788
150 ,900, 0.09, 0.1	0.6433868	0.66440513	3.267
175 ,700 ,0.12 ,0.2	0.6999128	0.70178787	0.268
175,900,0.09,0.15	0.6327041	0.66676657	5.384
175,1000,0.09,0.2	0.7923613	0.7852447	0.898
175, 1100, 0.09, 0.1	0.6896397	0.66995102	2.855
195 ,800 ,0.12 ,0.15	0.6341026	0.63290032	0.19
195 ,900, 0.12, 0.2	0.6634371	0.65801495	0.817
195, 1100,0.09,0.2	0.808517	0.79140182	2.117
195,1200,0.09,0.15	0.7499815	0.76108938	1.481

Finally, a multi-input – LP, SS, HS, and BD, multi-output – surface roughness and UTS neural network was developed with the training data and tested for error rate. The results show the achieved minimum error rate of 0.46% and the maximum error rate of 33.17% (Table 17). From the results, it is evident that for training a multi-input multi-output network, more data will need to be incorporated to make the model both more stable (lower loss function and more accurate weights in the trained function) and accurate.

Table 17: Surface roughness: actual vs predicted data with error percentage in multi-input multi-output neural network.

Training data	Actual Ra/100	Predicted Ra/100	Error %
125,700,0.09,0.1	0.2216	0.2075	6.34
125 ,800 ,0.09 ,0.2	0.1824	0.1352	25.88
150 ,800 ,0.09 ,0.2	0.1556	0.1458	6.32
150 ,900, 0.09, 0.1	0.1388	0.1848	33.17
175 ,700 ,0.12 ,0.2	0.1689	0.1829	8.31
175,900,0.09,0.15	0.1755	0.1691	3.67
175,1000,0.09,0.2	0.1547	0.1282	17.13
175, 1100, 0.09, 0.1	0.1635	0.1656	1.29
195 ,800 ,0.12 ,0.15	0.1968	0.1929	1.99
195 ,900, 0.12, 0.2	0.1382	0.1618	17.07
195, 1100,0.09,0.2	0.1447	0.1235	14.61
195,1200,0.09,0.15	0.1129	0.1347	19.28

Table 18: UTS: actual vs predicted data with percentage error in multi-input multi-output neural network.

Training data	Actual (UTS /1000)	Predicted (UTS /1000)	Error %
125,700,0.09,0.1	0.7168	0.6736	6.03
125 ,800 ,0.09 ,0.2	0.7752	0.8003	3.24
150 ,800 ,0.09 ,0.2	0.7793	0.7757	0.46
150 ,900, 0.09, 0.1	0.6434	0.6773	5.27
175 ,700 ,0.12 ,0.2	0.6999	0.6745	3.62
175,900,0.09,0.15	0.6327	0.7055	11.51
175,1000,0.09,0.2	0.7923	0.7799	1.58
175, 1100, 0.09, 0.1	0.6896	0.6809	1.27
195 ,800 ,0.12 ,0.15	0.6341	0.6276	1.02
195 ,900, 0.12, 0.2	0.6634	0.6837	3.05
195, 1100,0.09,0.2	0.8085	0.7741	4.26
195,1200,0.09,0.15	0.7499	0.7316	2.44

Comparing the results of models developed by SVR, RFR, and FFBP neural network revealed that SVR was not an ideal method for developing a predictive function since the error rate was not constant, which showed uncertainty inside the developed model (Table 13). RFR using three trees and a limited number of experiments led to a much more stable error rate compared to SVR.

Similarly, FFBP NN with a loss rate of 0.0002946 is more stable and accurate than SVR. Hence, in the future, we will employ both random forest and FFBP NN with more experimental data to study the uncertainty and minimize the error rate.

4. Conclusion and Future Works

In this work, a two-phase framework was proposed for optimizing the process parameters thereby achieving maximum density and better ultimate properties in parts manufactured by PBF. Next, the results were employed to develop a predictive model using different approaches to correlate a given set of process parameters, material properties, and ultimate quality properties.

In phase I, VED optimum range was obtained between 90 and 105 J/mm^3 to manufacture SS 316L parts with maximum density, the optimum range of laser power -- between 100 to 175 W, and optimum range of scan speed between 700 to 1000 mm/s. SA was conducted and the results showed that scan speed has the highest impact on VED, followed by laser power and hatch space respectively.

Porosity and microstructure analysis showed that the formation of gas pores and LOF pores led to high porosity percentage in both high and low VED ranges; whereas porosity reduced steeply in the optimum VED range -- mentioned previously -- with maximum density of 99.31% achieved for VED of 99.2 J/mm^3

In phase II, the impact of laser power, scan speed, hatch space, and beam diameter on surface roughness, hardness, impact strength, and ultimate tensile strength were studied. These results were employed to develop the correlation between the process parameters, material properties, and ultimate quality properties of the manufactured samples.

Analysis of surface roughness showed that the impact on roughness within the optimum VED range is in the following order: scan speed, laser power, hatch space, and beam diameter. The results also demonstrated that increasing scan speed or laser power decreased the average roughness. Also, the analysis of hardness results showed that the hardness of samples remained constant -- at the value of 90 ± 4 -- within the optimum VED range, regardless of the set of process parameters used for printing of the samples. Analysis of the impact strength demonstrated that the effect of the process parameters on the strength of the printed samples is in the following order: hatch space, laser power, scan speed, and then beam diameter, in a way that, increasing scan speed increased the impact strength. Whereas laser power and hatch space had an opposite effect no specific correlation was found between beam diameter and impact strength. Analysis of tensile test results demonstrated that the impact on UTS is in the following order: scan speed, beam diameter, laser power, and hatch space. More experiments have to be conducted within the optimized VED to gain an increased understanding of the correlation between process parameters and tensile properties.

Finally, we developed an intelligent model for prediction of surface roughness by using three different techniques: SVR, RFR, and FFBP NN. According to our results, FFBP NN includes the lowest mean error percentage rate of 10.25% amongst all of the techniques for surface roughness. Thus, this technique was used to develop the prediction model for UTS and achieved a mean error percentage rate of 7.53%. In the final step, the same technique was considered for developing a comprehensive multi-input multi-output predictive model with similar inputs, while considers both surface roughness and UTS as outputs. Analysis of results for the comprehensive predictive

model showed a mean error percentage 24.19% considering all outputs. However, this error is higher than multi-input single-output predictive model, which was expected given the limited amount of training data. We anticipate that the results can be improved by increasing the size of the training dataset.

The proposed framework demonstrates the capability of standardizing evaluation and optimizing process parameters while addressing important limitations in the literature, especially the statistical inconsistency in the impact of different parameters on the ultimate quality of printed samples. The developed multi-input model addressed one of the main challenges -- model uncertainty -- leading to process stability; however, the error rate was high. Using a larger dataset can eliminate this drawback.

Ongoing work includes incorporating more data in order to minimize the loss function and error rate and to improve the predictive accuracy. Next, we will merge all trained networks to provide a model correlating all controllable inputs to all outputs. The longer-term objective is to integrate the proposed framework within an online monitoring and control (OMC) system [2, 40]. This will make it possible to manufacture nearly flawless parts by using customized scan strategies to achieve desired ultimate qualities [41, 42]. Currently, a great deal of research has focused on the development of OMC systems [43, 44] to avoid/diminish the in-process defects and abnormalities [45, 46]. To fulfill such objective, real-time monitoring, and control of VED is the first step. This is because thermal specifications and the evolution of any inherently thermal AM process such as PBF have been found to be the predominant contributing factors affecting the microstructure and ultimate mechanical properties of manufactured parts [47, 48].

Moreover, real-time control of VED helps in manufacturing a more efficient topologically optimized support structure -- an efficient approach for reducing residual stress and distortion through facilitating conduction during the manufacturing process and increasing the structural strength. Using multi-laser PBF process allows manufacturers to use a laser with different power for manufacturing the support structures. Thus, it is possible to use different layer thickness/material for support structures. However, employment of such technique required adjusting VED for layers with different thickness or material with different thermal characteristics. Integration of the predictive model and OMC system will make this possible. Optimization of PBF process by using a predictive model – introduced in this project – integrated with an OMC system will be a breakthrough, which will considerably improve the mechanical properties and surface quality, increase the repeatability, reduce manufacturing lead time, and significantly decrease the need for the post-processing operations.

Acknowledgement

This research was supported by CAMRI (Collaborative Additive Manufacturing Research Institute) at Purdue School of Engineering and Technology, IUPUI. We would like to express our gratitude to Quad City Manufacturing Laboratory for supporting this project by conducting the experiments.

References

1. Dilberoglu, U.M., et al., *The role of additive manufacturing in the era of industry 4.0.* Procedia Manufacturing, 2017. **11**: p. 545-554.
2. Maleki Pour, E., *Innovative Tessellation Algorithm for Generating More Uniform Temperature Distribution in the Powder-bed Fusion Process*. 2018.
3. Malekipour, E. and H. El-Mounayri, *Common defects and contributing parameters in powder bed fusion AM process and their classification for online monitoring and control: a review.* The International Journal of Advanced Manufacturing Technology, 2018. **95**(1-4): p. 527-550.
4. DebRoy, T., et al., *Additive manufacturing of metallic components–process, structure and properties.* Progress in Materials Science, 2018. **92**: p. 112-224.
5. Brown, C.U., et al., *The effects of laser powder bed fusion process parameters on material hardness and density for nickel alloy 625*. 2018: US Department of Commerce, National Institute of Standards and Technology.
6. Oliveira, J.P., A. LaLonde, and J. Ma, *Processing parameters in laser powder bed fusion metal additive manufacturing.* Materials & Design, 2020. **193**: p. 108762.
7. Yan, W., et al., *Data-driven multi-scale multi-physics models to derive process–structure–property relationships for additive manufacturing.* Computational Mechanics, 2018. **61**(5): p. 521-541.
8. Malekipour, E. and H. El-Mounayri, *Defects, process parameters and signatures for online monitoring and control in powder-based additive manufacturing*, in *Mechanics of Additive and Advanced Manufacturing, Volume 9*. 2018, Springer. p. 83-90.
9. Liverani, E., et al., *Effect of selective laser melting (SLM) process parameters on microstructure and mechanical properties of 316L austenitic stainless steel.* Journal of Materials Processing Technology, 2017. **249**: p. 255-263.
10. Sun, Z., et al., *Selective laser melting of stainless steel 316L with low porosity and high build rates.* Materials & Design, 2016. **104**: p. 197-204.
11. Bertoli, U.S., et al., *On the limitations of volumetric energy density as a design parameter for selective laser melting.* Materials & Design, 2017. **113**: p. 331-340.
12. Guan, K., et al., *Effects of processing parameters on tensile properties of selective laser melted 304 stainless steel.* Materials & Design, 2013. **50**: p. 581-586.
13. Vandenbroucke, B. and J.P. Kruth, *Selective laser melting of biocompatible metals for rapid manufacturing of medical parts.* Rapid Prototyping Journal, 2007.
14. Abele, E., et al., *Selective laser melting for manufacturing of thin-walled porous elements.* Journal of Materials Processing Technology, 2015. **215**: p. 114-122.
15. Malekipour, E., et al., *Predicting Temperature Field in PBF process Using Radial Basis Neural Network (RBNN).*
16. Malekipour, E., et al., *An Innovative Fast Layer-wise Simulation of Temperature distribution using a Chessboard Strategy (FALS TECHS) in the Powder-bed Fusion Process.* Additive Manufacturing, 2021: p. 102065.
17. Akbari, A., D. Wang, and J. Chen, *Peak loads on teeth from a generic mouthpiece of a vibration device for accelerating tooth movement.* American Journal of Orthodontics and Dentofacial Orthopedics, 2021.
18. Cherry, J., et al., *Investigation into the effect of process parameters on microstructural and physical properties of 316L stainless steel parts by selective laser melting.* The International Journal of Advanced Manufacturing Technology, 2015. **76**(5-8): p. 869-879.

19. Bassoli, E., et al., *Development of laser-based powder bed fusion process parameters and scanning strategy for new metal alloy grades: A holistic method formulation.* Materials, 2018. **11**(12): p. 2356.
20. Cheng, B. and K. Chou. *Melt pool evolution study in selective laser melting*. in *26th Annual International Solid Freeform Fabrication Symposium-An Additive Manufacturing Conference, Austin, TX, USA*. 2015.
21. Hamby, D.M., *A review of techniques for parameter sensitivity analysis of environmental models.* Environmental monitoring and assessment, 1994. **32**(2): p. 135-154.
22. Van Elsen, M., *Complexity of Selective Laser Melting: a new optimisation approach.* 2007.
23. Ruban, W., et al., *Effective process parameters in selective laser sintering.* International Journal of Rapid Manufacturing, 2014. **4**(2-4): p. 148-164.
24. Gu, D. and Y. Shen, *Processing conditions and microstructural features of porous 316L stainless steel components by DMLS.* Applied Surface Science, 2008. **255**(5): p. 1880-1887.
25. Sufiiarov, V.S., et al., *The effect of layer thickness at selective laser melting.* Procedia engineering, 2017. **174**: p. 126-134.
26. du Plessis, A., *Effects of process parameters on porosity in laser powder bed fusion revealed by X-ray tomography.* Additive Manufacturing, 2019. **30**: p. 100871.
27. Petrousek, P., et al., *Influence of Cryorolling on Properties of L-PBF 316L Stainless Steel Tested at 298K and 77K.* Acta Metallurgica Slovaca, 2019. **25**(4): p. 283-290.
28. Khorasani, M., et al., *On the role of process parameters on meltpool temperature and tensile properties of stainless steel 316L produced by powder bed fusion.* journal of materials research and technology, 2021. **12**: p. 2438-2452.
29. Gangireddy, S., et al., *Microstructure and mechanical behavior of an additive manufactured (AM) WE43-Mg alloy.* Additive Manufacturing, 2019. **26**: p. 53-64.
30. Palanivel, S., et al., *Spatially dependent properties in a laser additive manufactured Ti–6Al–4V component.* Materials Science and Engineering: A, 2016. **654**: p. 39-52.
31. E8M-14, A.E., *Standard Test Methods for Tension Testing of Metallic Materials, ASTM International, West Conshohocken, PA, 2013,* www.astm.org. ASTM International.
32. Chen, H., *A process modelling and parameters optimization and recommendation system for binder jetting additive manufacturing process*. 2016: McGill University (Canada).
33. Campanelli, S.L., et al., *Capabilities and performances of the selective laser melting process.* New Trends in Technologies: Devices, Computer, Communication and Industrial Systems, 2010. **1**(1): p. 233-252.
34. Kruth, J.-P., et al., *Consolidation phenomena in laser and powder-bed based layered manufacturing.* CIRP annals, 2007. **56**(2): p. 730-759.
35. Moshagen, T., N.A. Adde, and A.N. Rajgopal, *Finding hidden-feature depending laws inside a data set and classifying it using Neural Network.* arXiv preprint arXiv:2101.10427, 2021.
36. Wolff, S.J., et al., *A framework to link localized cooling and properties of directed energy deposition (DED)-processed Ti-6Al-4V.* Acta Materialia, 2017. **132**: p. 106-117.
37. Marrey, M., et al., *A framework for optimizing process parameters in powder bed fusion (pbf) process using artificial neural network (ann).* Procedia Manufacturing, 2019. **34**: p. 505-515.
38. Yan, F., W. Xiong, and E.J. Faierson, *Grain structure control of additively manufactured metallic materials.* Materials, 2017. **10**(11): p. 1260.
39. Eshkabilov, S., et al., *Mechanical and thermal properties of stainless steel parts, manufactured by various technologies, in relation to their microstructure.* International Journal of Engineering Science, 2021. **159**: p. 103398.
40. Malekipour, E., et al., *A Vision toward Layer-wise Intelligent Monitoring and Control of Scan Strategy in Powderbed Fusion Process.* TechConnect Briefs, 2019: p. 127-130.
41. Malekipour, E. and H. El-Mounayri. *Scanning Strategies in the PBF Process: A Critical Review*. in *ASME International Mechanical Engineering Congress and Exposition*. 2020. American Society of Mechanical Engineers.
42. Malekipour, E., et al. *Optimization of Chessboard Scanning Strategy Using Genetic Algorithm in Multi-Laser Additive Manufacturing Process*. in *ASME International Mechanical Engineering Congress and Exposition*. 2020. American Society of Mechanical Engineers.
43. Amini, M. and S. Chang, *Process Monitoring of 3D Metal Printing in Industrial Scale.* 2018(51357): p. V001T01A035.
44. Imani, F., et al. *Layerwise in-process quality monitoring in laser powder bed fusion*. in *International Manufacturing Science and Engineering Conference*. 2018. American Society of Mechanical Engineers.
45. Taheri, H., et al., *Powder-based additive manufacturing–a review of types of defects, generation mechanisms, detection, property evaluation and metrology.* 2017. **1**(2): p. 172.
46. Montazeri, M., et al., *In-process monitoring of material cross-contamination defects in laser powder bed fusion.* Journal of Manufacturing Science and Engineering, 2018. **140**(11): p. 111001.
47. Attoye, S., E. Malekipour, and H. El-Mounayri. *Correlation Between Process Parameters and Mechanical Properties in Parts Printed by the Fused Deposition Modeling Process*. in *Mechanics of Additive and Advanced Manufacturing, Volume 8*. 2019. Cham: Springer International Publishing.
48. Malekipour, E., S. Attoye, and H. El-Mounayri, *Investigation of layer based thermal behavior in fused deposition modeling process by infrared thermography.* Procedia Manufacturing, 2018. **26**: p. 1014-1022.